Initialization of a Cloud-Resolving Model with Airborne Doppler Radar Observations of an Oceanic Tropical Convective System

SOLINE BIELLI AND FRANK ROUX

Laboratoire d'Aérologie, UMR CNRS—Université Paul Sabatier, Toulouse, France

(Manuscript received 11 September 1997, in final form 8 June 1998)

ABSTRACT

Doppler radar–derived fields of wind and reflectivity, retrieved temperature perturbations, estimated water vapor, and cloud water contents are used to initialize a nonhydrostatic cloud-resolving model. Airborne Doppler data collected in a tropical mesoscale convective system on 9 February 1993 during the Tropical Ocean Global Atmosphere Coupled Ocean–Atmosphere Response Experiment are prepared for this purpose. Different numerical experiments are conducted to verify the reliability of the approach and to determine the most important parameters leading to the most realistic simulations possible.

The obtained results show that the numerical model can be initialized with two-dimensional wind and reflectivity fields describing a well-developed convective circulation. A major conclusion is that, apart from the horizontal and vertical wind, the most important parameter in the initial field is humidity. Although a relatively crude thermodynamic and microphysical description was sufficient, a complete description of the saturated/unsaturated conditions is essential to obtain simulations matching the observed characteristics. Finally, consequences of the results for the understanding of the 9 February 1993 mesoscale convective system and future applications of this technique are discussed.

1. Introduction

Observational and numerical approaches have been extensively used to study mesoscale convective systems (MCSs) in the Tropics and the midlatitudes, over the continents and the oceans. Since the 1970s ground-based and airborne Doppler radar have been increasingly used to investigate MCSs. Doppler radar is now a proven technique to observe the air motions in precipitating convective and stratiform clouds. During the same period, cloud-resolving models (CRMs) have achieved a high degree of sophistication and realism, and are powerful tools to investigate the physical mechanisms involved in the generation, maintenance, and evolution of MCSs and for sensitivity studies. It is now recognized that both observational and numerical approaches can provide detailed information on mesoscale precipitating systems, with their own advantages and limitations.

Radar observations provide reflectivity and radial velocity data, from which three-dimensional fields of Cartesian wind components and precipitating water contents can be derived. Moreover, thermodynamic (pressure and temperature) and microphysical (water vapor, precipitating and nonprecipitating water contents) fields can be ''retrieved'' from these results [see, e.g., Houze (1993) for a review]. But these analyses can be conducted only in regions of the atmosphere where there are enough hydrometeors to return a detectable signal. These areas include most, but not all, of the dynamically active part of the atmospheric perturbations, but they miss the less active, cloud-free environment.

CRMs generate time series of complete sets of variables within a predefined two- or three-dimensional domain where precipitating and nonprecipitating regions coexist [see, e.g., Emanuel (1994) for a review]. But, to initialize numerical simulations, simplified and rather unrealistic assumptions have to be made. Artificial (positive or negative) thermal perturbations, which often contain considerable amounts of energy, are superimposed on horizontally homogeneous fields derived from radiosounding data. At the earliest simulated times, this usually leads to unrealistic features. However, later results of CRMs have been shown to agree well with observations for various meteorological situations, although the dependence of simulated evolution on the initial conditions cannot be completely ruled out. Emanuel (1994) pointed out that the initial convective instability must be rather large for clouds to develop and that tropical soundings are not usually unstable enough to generate convection.

Lilly (1990) discussed a number of difficulties in nu-

Corresponding author's address: Frank Roux, Laboratoire d'Aérologie, Observatoire Midi-Pyrénées, 14 avenue Edouard Belin, 31400 Toulouse, France.
E-mail: bies@aero.obs-mip.fr

merical prediction at the convective scale, particularly the need for methods to initialize convective models with observational data. In this framework, Lin et al. (1993) were the first to develop a method to initialize a numerical simulation with Doppler radar-derived fields. They established the feasibility of the method using radar data from the 20 May 1977 Del City tornadic supercell storm and obtained encouraging results. Despite some discrepancies in the evolution of the observed and simulated storms, the results suggested that initialization of numerical models with radar observations, instead of radiosounding data only, does improve the model's ability to predict the behavior of the storm. They concluded that further experiments are needed to more generally assess the applicability of such an approach for different meteorological situations. Likewise, Crook (1994) and Crook and Tuttle (1994) used radar-derived winds to initialize numerical simulations of gust-front cases. These studies concentrated on the dry boundary layer because of its simpler dynamics. They also obtained satisfying results on the model's ability to predict the motion of gust fronts, although they recognized that more experiments are needed to validate this approach, especially for moist convective flows. More recently, Sun and Crook (1997, 1998) developed a 4D variational data assimilation technique to retrieve 3D wind, thermodynamical, and microphysical fields from a time series of radar-observed radial velocities and reflectivities, through the minimization of a cost function defined by the difference between the radar observations and their model prediction. The authors showed that detailed cloud structures in simulated and observed convective storms could be retrieved by this method using information from Doppler radars. They noted, however, that poor representation of moist processes and water contents could have a large impact on the retrieval.

We follow here a different and simpler approach: Doppler-derived fields are used to determine initial conditions from which a cloud-resolving numerical model is started. Our goal is to examine the relative importance of the different quantities that can be calculated, retrieved, or estimated from the radar data based on qualitative comparisons between the observed and simulated fields. To this purpose, we use airborne Doppler data concerning the oceanic tropical MCS observed on 9 February 1993 during the Tropical Ocean Global Atmosphere Coupled Ocean–Atmosphere Response Experiment (TOGA COARE) (Webster and Lukas 1992). These data have been previously analyzed by LeMone et al. (1994), Smull et al. (1994, 1995, 1996), Lee and Hildebrand (1995, 1996), Roux (1995), Hildebrand et al. (1996), and Jorgensen et al. (1996). A more detailed description of the MCS structure, evolution, and associated budgets, as well as indications on the methods used to analyze the data, can be found in Roux (1998). The numerical cloud model used here is the MESO-NH Atmospheric Simulation System (hereafter MESO-NH; Lafore et al. 1998) currently developed by Centre National de Recherches Météorologiques (CNRM, Météo-France, Toulouse, France) and Laboratoire d'Aérologie (LA, Centre National de la Recherche Scientifique, Toulouse, France).

A series of numerical simulations has been performed to examine the response of the model to different initial states. In section 2, we review the environmental conditions within which the 9 February 1993 system developed and the main characteristics of the radar-derived fields. In section 3, the model used in this study is briefly presented. Section 4 explains the different initial states used for the numerical experiments, the results of which are detailed in section 5. Section 6 deals with conclusions that can be drawn from the obtained results and with future applications of this technique.

2. The 9 February 1993 mesoscale convective system

A detailed description of the MCS observed on 9 February 1993 from 1600 till 2155 (all times are UTC, local time is UTC + 11) during TOGA COARE, as derived mainly from airborne Doppler data, can be found in Roux (1998) and only its main characteristics will be presented here. This MCS was a class-3 system (see Webster and Lukas 1992): the associated area of infrared cloud-top temperature smaller than 208 K reached a maximum extent of 40 000 km^2. It was observed during a period of low-level westerly winds and over an area of sea surface temperature greater than 29°C. In fact, this MCS was a part of a cloud cluster that could be identified on the satellite images from 0945 till 2345. It was located near 4°S, 159.5°E, southeast of the TOGA COARE Intensive Flux Array. At the mature stage (1700–1900), it was composed of a line of cumulonimbus at the north and more stratiform precipitation to the south. It propagated northward at 5 m s^{-1}.

A composite sounding (Fig. 1a) was deduced from upper-level data of the R/V *Shiyan* (2.39°S, 158.32°E) radiosounding at 1700 and National Oceanic and Atmospheric Administration (NOAA) P3 N43RF flight-level measurements at 1544–1602 near 5.75°S, 160°E below 4800 m. The large-scale environment was characterized by moderate low-level westerlies ($\leq$7 m s^{-1}) overlaid by easterlies above 500 hPa ($>$20 m s^{-1} above 200 hPa) (Fig. 1b). The MCS major axis (112°–292°) was aligned approximately parallel to the wind shear above 2-km altitude (2×10^{-3} s^{-1} from 95°), but more perpendicular to that below 2 km (3.4×10^{-3} s^{-1} from 235°).

The atmosphere was very moist up to 10-km altitude ($T - T_D$ was less than 5°C), and was convectively unstable. When considering a 50-hPa deep layer above surface, using virtual potential temperature to calculate thermal buoyancy and supposing that the air parcels remain undiluted during ascent, the lifting condensation level (LCL) was at 0.6-km altitude, the level of free convection at 1.3 km, and the equilibrium temperature

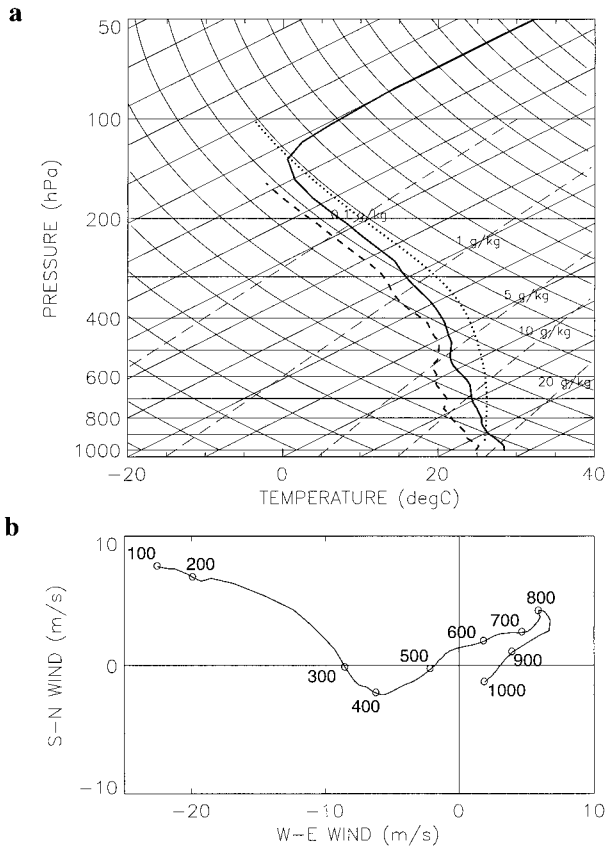

FIG. 1. Composite sounding based on the radiosonde launched from R/V *Shiyan 3* at 1700 and P3 N43RF flight-level measurements (a) skew *T*–log*p* diagram, (b) wind hodograph (the different levels are indicated in hPa).

level at 14.8 km. The convective available potential energy (CAPE) value was 1663 J kg^{-1} and the convective inhibition was -18 J kg^{-1}. These values are typical of the environment of oceanic tropical convection. Three factors can substantially modify them: the depth of the potentially unstable layer (referred to as H, in hPa), the weight of liquid water above LCL (q_c in g kg^{-1}), and the entrainment rate of environmental air [$\lambda = (1/M)\partial M/\partial z$, in 10^{-2} km^{-1}, where M is the vertical mass flux]. Different tests with the sounding displayed in Fig. 1 have revealed that the CAPE sensitivity with respect to these three factors was

$$\frac{\partial \text{CAPE}}{\partial H} \approx -10 \text{ (J kg}^{-1}\text{) (hPa)}^{-1},$$

$$\frac{\partial \text{CAPE}}{\partial q_c} \approx -135 \text{ (J kg}^{-1}\text{) (g kg}^{-1}\text{)}^{-1},$$

$$\frac{\partial \text{CAPE}}{\partial \lambda} \approx -75 \text{ (J kg}^{-1}\text{) (10}^{-2} \text{ km}^{-1}\text{)}^{-1}.$$

Considering realistic values of $H = 70$ hPa, $\lambda = 10^{-2}$ km^{-1}, $q_c = 1$ g kg^{-1}, the CAPE value reduces to 1450 J kg^{-1}.

Three-dimensional fields of reflectivity and Cartesian wind components in the frame moving with the MCS propagation (5 m s^{-1} northward) were deduced from data collected with the Doppler radars aboard the two NOAA P3s and the National Center for Atmospheric Research NCAR Electra aircraft during the period 1635–1905. The MCS-relative horizontal airflow showed a confluence zone along the system's northern edge and a predominantly along-line flow. The more or less transient regions of most intense upward motions and reflectivity values were approximately aligned along the northern edge.

Representative cross-line circulations were calculated from the Doppler-derived three-dimensional wind and reflectivity fields to determine initial conditions from which the model is started. First, a mean cross section was deduced from an average of the velocity components and reflectivity-derived precipitation contents over 80-km length in along-line direction (112°–292° east from north). Then, data void regions were filled with environmental winds deduced from the composite hodograph. An iterative filtering procedure (Cressman 1959) was applied only to the extrapolated values, so as to ensure continuity with the radar-derived values. Then, wind components exactly verifying the two-dimensional (cross-line) continuity equation were derived from a variational analysis using a streamfunction. A similar method was used by Hauser et al. (1988) and Roux et al. (1993) in their study of a West African squall line and a narrow cold-frontal rainband, respectively.

The results of this analysis are shown in Fig. 2. In the vertical, two main horizontal flows were observed: a mid-to-upper-level, front-to-rear (FTR, southward, right-to-left) flow and a weaker low-level, rear-to-front (RTF, northward, left-to-right) flow. The updraft in the FTR flow reached a maximum intensity of 4 m s^{-1} at 10-km altitude, it was followed by a downdraft of -2 m s^{-1} maximum intensity feeding the RTF flow. The vertical circulation in the cross-line direction was evolving. At the earliest times, the upward motions were intense and relatively high reflectivity values (>40 dBZ) were observed. Then, upward motions and reflectivity progressively decreased. A secondary reflectivity maximum appeared near the level of the 0°C isotherm (at about 5 km) in the southern part of the system. This ''brightband'' signature is due to melting hydrometeors and is characteristic of MCS's stratiform regions.

Temperature and pressure perturbations were also retrieved from the two-dimensional wind and reflectivity fields shown in Fig. 2 through a method derived from that used by Roux et al. (1993). As seen in Fig. 3, the FTR and RTF flows were found warmer and colder, respectively, than the environment. The mean temperature perturbations were less than ± 1 K, which are typical values for tropical oceanic convection. With time, as did the intensity of the vertical motions, the thermodynamic contrast between both flows progressively lessened. A more complete discussion of the thermo-

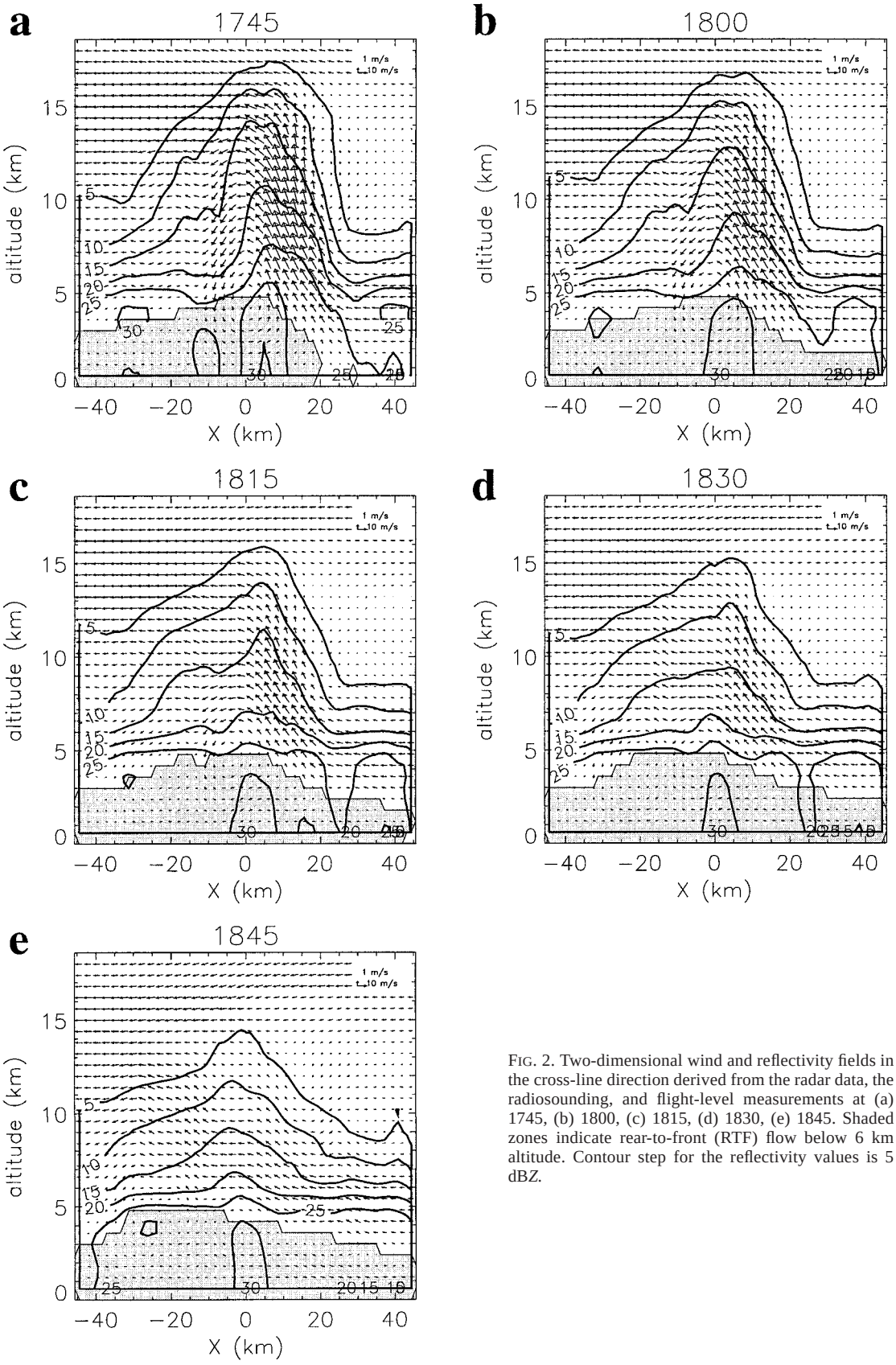

FIG. 2. Two-dimensional wind and reflectivity fields in the cross-line direction derived from the radar data, the radiosounding, and flight-level measurements at (a) 1745, (b) 1800, (c) 1815, (d) 1830, (e) 1845. Shaded zones indicate rear-to-front (RTF) flow below 6 km altitude. Contour step for the reflectivity values is 5 dBZ.

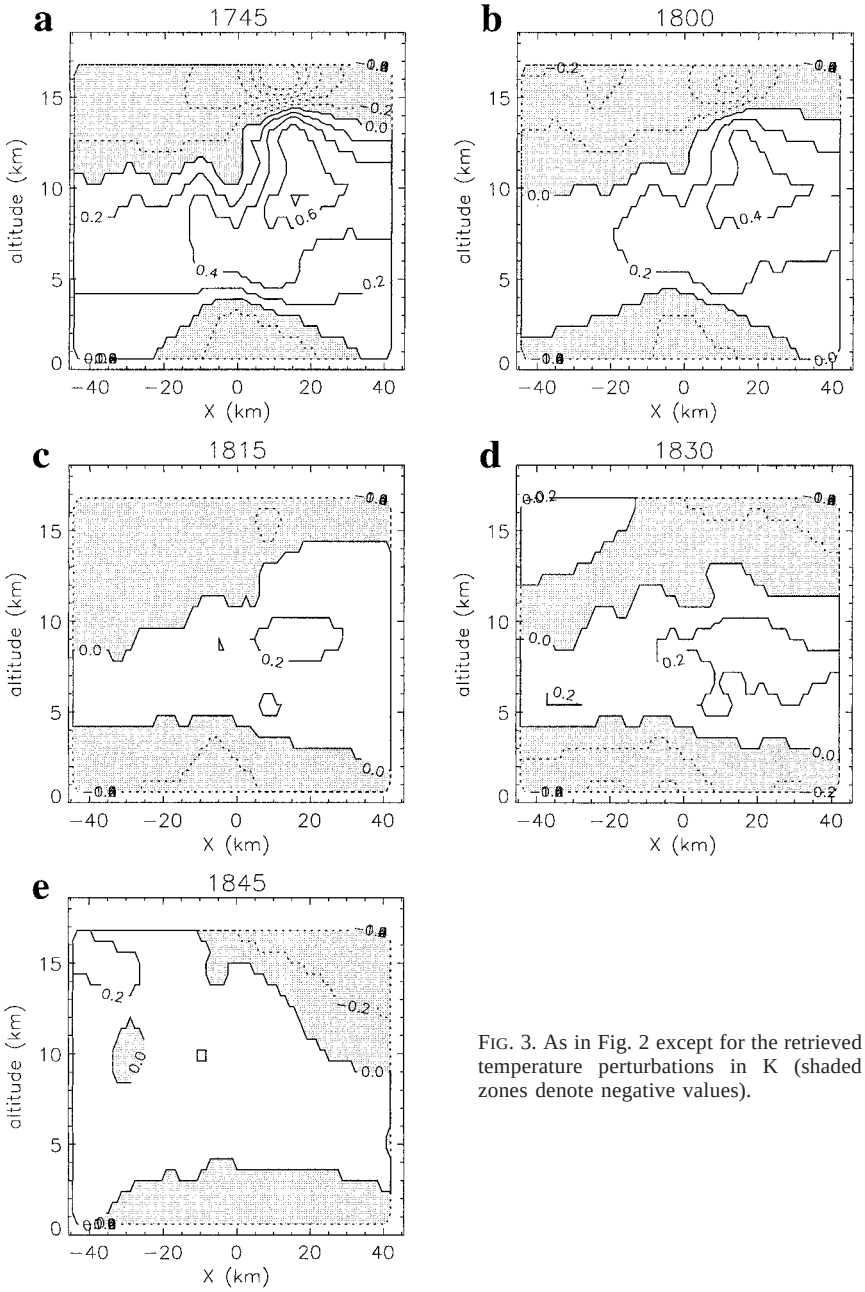

FIG. 3. As in Fig. 2 except for the retrieved temperature perturbations in K (shaded zones denote negative values).

dynamic structure and evolution of the 9 February 1993 MCS derived from the retrieved fields can be found in Roux (1998).

3. The MESO-NH model

MESO-NH is the result of a joint effort of CNRM and LA. This nonhydrostatic model is based on the Lipps and Hemler (1982) modified anelastic system. The basic atmospheric variables are temperature, pressure, total density of moist air, and density of the dry fraction of the air. The prognostic variables of the model are the three Cartesian components of velocity, the dry potential temperature, and the different water mixing ratios. The ''warm'' (liquid phase) microphysical processes are parameterized following Kessler (1969). Three categories of ice (cloud ice, snow, and graupel) are used to account for the ''cold'' microphysical processes (Pinty 1997).

In all simulations, a stretched vertical coordinate was used in order to maximize resolution in the lowest of the 43 levels of the model. Close to the surface, the resolution was 100 m; it progressively increased to 600 m at 1.2-km altitude and higher. For display purposes, the simulated fields were interpolated to a regular ver-

tical grid with a 600-m spacing. Rigid boundary and free-slip conditions were applied at the bottom and top of the domain, respectively, with a sponge layer above 17 km to minimize the reflection of internal gravity waves from the rigid upper boundary. The x axis was taken normal to the MCS line (positive 22° east from north) and open lateral boundary conditions were chosen. In the radar-derived and simulated wind fields, the storm translation speed (5 m s^{-1} northward) was subtracted from the initial wind field so that the observed and simulated cloud remained within the domain throughout the considered period.

The horizontal dimension of the considered domain was 80 km with a grid spacing Δ_m of 3.6 km. This relatively coarse grid size was chosen to fit the estimated spectral characteristics of the radar-derived fields. As shown in Roux and Sun (1990), horizontal wavelengths smaller than $6\Delta_r$, where Δ_r is the horizontal grid spacing from the radar-derived fields, are filtered out during the analysis. Hence, as a grid spacing Δ_r of 1.8 km was used for the Doppler-derived three-dimensional wind and reflectivity fields (from which the two-dimensional fields were obtained), and considering the Shannon sampling theorem (which implies that only wavelengths larger than $3\Delta_r$ can be explicitely represented), a grid spacing Δ_m of 3.6 km was chosen for the numerical simulations. As shown below, slightly smaller grid spacing Δ_m could be used. However, we found that, for Δ_m smaller than about 2 km, wind oscillations developed and amplified rapidly at the beginning of the simulation, in regions of strong velocity gradient. Their influence on the ''smooth'' initial flow led to simulated circulations bearing little resemblance with the observed ones. It is also to be noted that Weisman et al. (1997) found that, in nonhydrostatic model simulations, resolutions as coarse as 4 km are sufficient to reproduce much of the mesoscale structure and evolution of squall line type convective system produced in 1-km simulations. In this study, we focused on the convective part of the system where most of the airborne Doppler observations were conducted. Hence, the size of the considered domain was relatively small (80 km horizontally) and the physical processes leading to the development of an extensive stratiform anvil were not considered.

The two-dimensional assumption was not necessarily realistic, but it was justified to the extent that the variations in kinematic and dynamic quantities were much greater in the line-normal direction than in the line-parallel one. Through a comparison between two- and three-dimensional simulations of a tropical squall line, Nicholls and Weissbluth (1988) showed that the main dynamical and microphysical characteristics can be captured in the two-dimensional framework. However, this may impose some restrictions in the model's ability to simulate certain features. In particular, a turning wind shear, which can be important to determine the structure and evolution of MCS, cannot be simulated (Barnes and Sieckman 1984). Concerning the 9 February 1993 MCS, although the mean tropospheric wind shear was almost parallel to the line orientation (but the low-level shear was more perpendicular), the radar-derived wind and reflectivity fields showed rather homogeneous features in the along-line direction (Roux 1998).

4. Initial conditions and experiment design

We present here the series of experiments with different initial conditions and model configurations that were designed to examine different ways to initialize a numerical model with radar observations. Note that, for all the numerical experiments described below, no large-scale forcing was imposed and the Coriolis force was not taken into account as the observed MCS occurred very close to the equator, between 3.5° and 5°S.

a. Initial conditions

The initial temperature and moisture conditions for the simulations were deduced from the composite sounding shown in Fig. 1. The environmental humidity profile was used in a first series of simulations. Then different modifications of the humidity distribution were tested in order to more accurately represent the internal characteristics of the MCS. First, all the regions where precipitation were observed with radar (i.e., where the reflectivity values were above 0 dBZ) were supposed to be saturated, while environmental mixing ratio was kept unmodified in the precipitation-free zones. Second, an attempt was made to distinguish the saturated from the unsaturated zones.

Although numerical techniques to retrieve humidity (and other water variables) from Doppler radar data have been developed (e.g., Rutledge and Hobbs 1983; Hauser et al. 1988; Geerts and Hobbs 1991), their use is more problematic than that of the simpler dynamic–thermodynamic retrieval technique (like that used to retrieve the temperature perturbations in Fig. 3) owing to the delicate balance that needs to be verified between internal source/sink terms, boundary conditions, and evolution. Hence, we chose to a priori specify the initial relative humidity fields with only two values representing saturated and unsaturated situations. Although it was not possible to directly deduce the water vapor and cloud water contents from the radar data, some indications could be obtained from the ''production rate of precipitation'' $F(q_p)$. This quantity was calculated from the precipitation content q_p (in g kg^{-1}) and the fall speed velocity V_p (in m s^{-1}) derived from the reflectivity values as

$$q_p = \frac{1}{\rho} a Z^b \quad \text{and} \quad V_p = \left(\frac{\rho}{\rho_0}\right)^{0.4} c Z^d,$$

where coefficients a, b, c, and d depend on the hydrometeor types, Z is the radar reflectivity (in mm^6 m^{-3}), and ρ and ρ_0 the air density at considered altitude and

TABLE 1. Characteristics of the different simulations.

Simulation	Initial wind field	Initial thermodynamic field	Initial perturbation	Microphysics	Model, Δm	Others
CLAS1	Environment	(Tenv, Qvenv)	Warm bubble	Liquid + ice	3D, 3.6 km	NO
CLAS2	Environment	(Tenv, Qvenv)	Cold bubbles	Liquid + ice	3D, 3.6 km	NO
CLAS3	Environment	(Tenv, Qvenv)	Cold source (20 min)	Liquid + ice	3D, 3.6 km	NO
WIND	Radar	(Tenv, Qvenv)	NO	Liquid + ice	2D, 3.6 km	NO
WIND + TEMP	Radar	(Tretrieved, Qvenv)	NO	Liquid + ice	2D, 3.6 km	NO
QVSAT	Radar	(Tenv, Qvsat)	NO	Liquid + ice	2D, 3.6 km	NO
QVSAT + TEMP	Radar	(Tretrieved, Qvsat)	NO	Liquid + ice	2D, 3.6 km	NO
QVSAT + CLOUD	Radar	(Tenv, Qvsat, Qc)	NO	Liquid + ice	2D, 3.6 km	NO
CONTROL	Radar	(Tenv, Qsat/nsat)	NO	Liquid + ice	2D, 3.6 km	NO
CONTROL-2.4	Radar	(Tenv, Qsat/nsat)	NO	Liquid + ice	2D, 2.4 km	NO
NOICE	Radar	(Tenv, Qsat/nsat)	NO	Liquid	2D, 3.6 km	NO
TEMP	Radar	(Tretrieved, Qsat/nsat)	NO	Liquid + ice	2D, 3.6 km	NO
CLOUD	Radar	(Tenv, Qsat/nsat, Qc)	NO	Liquid + ice	2D, 3.6 km	NO
SFLUX	Radar	(Tenv, Qsat/nsat)	NO	Liquid + ice	2D, 3.6 km	Surface flux
RAD	Radar	(Tenv, Qsat/nsat)	NO	Liquid + ice	2D, 3.6 km	Radiation

surface level, respectively. We used the same relations as Gamache et al. (1993), with the following values:

liquid hydrometeors ($T > 0$°C):

$$a = 1.33 \times 10^{-3} \qquad b = 0.69$$
$$c = -3.05 \qquad d = 0.05;$$

iced hydrometeors ($T < -10$°C):

$$a = 2.64 \times 10^{-3} \qquad b = 0.56$$
$$c = -0.817 \qquad d = 0.063.$$

A linear interpolation was used where the environmental temperature T was between $-10°$ and 0°C, a region where supercooled water might exist within updrafts. We have

$$F(q_p) = \frac{\partial q_p}{\partial t} + (\underline{V}\,\underline{\nabla})q_p + \frac{1}{\rho}\frac{\partial}{\partial z}(\rho V_p q_p) - \underline{\nabla}(\kappa \underline{\nabla} q_p),$$

where κ is the subgrid-scale dissipation rate, derived from the radar-derived velocity values as in Deardorff (1975) and Smagorinsky (1963). Here $F(q_p)$ gives an indication for saturation: negative values denote a precipitation sink, revealing that hydrometeors evaporate in unsaturated air, while positive values show that precipitation forms from cloud droplets or small ice crystals, which implies that air is saturated. Within the region where precipitation was observed, the relative humidity was assumed to be 100%, except where $F(q_p)$ was significantly negative (<-0.5 g kg^{-1} h^{-1}) and an 80% relative humidity was considered. As shown in Roux (1998), the only region where $F(q_p)$ was significantly negative was within the low-level RTF flow. Hence, the only precipitating region where air was supposed to be initially unsaturated was the low-level RTF flow. The environmental values of humidity were kept in the precipitation-free zones.

For the simulations with an initial cloud water content, following Willoughby et al. (1985), the cloud mixing ratio was assumed to be 0.5 g kg^{-1} below 5-km altitude and was taken as a linearly decreasing function of height above, in regions where the radar reflectivity values were larger than 0 dBZ and the production rate of precipitation was positive. Everywhere else, the cloud water content was assumed to be zero.

b. Experiment design

Fifteen simulations are discussed below in order to test the initialization of the MESO-NH numerical model with radar-derived wind and precipitating fields (Table 1). Concerning simulations with radar-derived values, the model was initialized with the two-dimensional circulation at 1745 and the following ones were used for comparisons between the model- and radar-derived fields.

Three runs were performed using environmental values only. Two simulations were initialized with a classical method: 1) a 40-km-wide and 2-km-deep bubble 5°C warmer than the environment centered at 1-km altitude (run CLAS1), and 2) a cold temperature anomaly, which is the aggregate of three overlapping bubbles of 20-km diameter and 2-km depth with a temperature deficit of 5°C centered at 5-km altitude (run CLAS2), were inserted at the center of the domain into a horizontally homogeneous environment to trigger convection. A third experiment was identical to CLAS2, except the cooling was maintained during 20 min (simulation CLAS3).

Simulation WIND was conducted with the Doppler-derived winds and the environmental thermodynamic characteristics. In experiment WIND + TEMP, the retrieved temperature perturbations were added to the environmental ones. Run QVSAT was identical to WIND, except that a saturated mixing ratio was imposed in the region where radar observations reveal the presence of precipitation. In simulations QVSAT + TEMP and QVSAT + CLOUD, retrieved temperature perturbations

and specifed cloud water contents were, respectively, added. The CONTROL experiment was identical to the QVSAT one, except that, as discussed above, the mixing ratio was reduced to 80% in the regions where the production rate of precipitation was negative. Run CONTROL-2.4 was identical, except a 2.4-km instead of 3.6-km grid spacing was used.

Simulation NOICE was run to study the impact of the ice phase: it had the same characteristics as the CONTROL experiment, except only the warm (liquid phase) microphysics was used. Simulation TEMP was conducted to test the sensitivity of the model to initial temperature perturbations: the initial state was the same as for the CONTROL experiment, but with temperature perturbations retrieved from Doppler data being added. Simulation CLOUD was performed with the same basic state as the CONTROL run, but with a vertically varying cloud content.

Two additional experiments were designed to examine the impact of radiation and surface heat and moisture fluxes to the dynamics of the MCS. In experiment RAD, the radiation scheme (Morcrette 1990) was activated after 2 h of the control simulation. In experiment SFLUX, the surface fluxes scheme, which uses a constant heat transfer coefficient and the near-surface wind speed (Charnock 1955), was activated at the beginning of the simulation with a constant sea surface temperature of 29.5°C. Otherwise these experiments were the same as the CONTROL run.

The quality of the simulations was subjectively estimated through comparisons with the observed fields (Figs. 2 and 3). As a matter of fact, although the structure and evolution of the simulated wind and hydrometeor fields can be compared qualitatively to the observed ones, it is much more difficult to quantitatively assess the reliability of the numerical results as two-dimensional simulations may differ substantially from two-dimensional averages of three-dimensional fields.

5. Results

a. Classical simulations

The results of the classical initializations (simulations CLAS1 and CLAS2, not shown) were rather disappointing. Vertical motions developed and shallow clouds formed as the warm or cold bubbles displaced vertically, but these features vanished soon after the bubbles reached their equilibrium levels, and no deep and long-lasting convective circulation could be maintained. Redelsperger and Lafore (1988) have already found that warm bubbles are not very efficient to initialize a squall line–type simulation.

Concerning initialization with a cold source, initial forcing was maintained for 20 min (simulation CLAS3). In this case again, shallow convection developed, but as soon as forced cooling was turned out, the vertical motions collapsed.

b. Simulation WIND

This simulation was conducted using the Doppler-derived wind field and the environmental thermodynamic characteristics (simulation WIND). In this case, vertical motions and water contents were only transient features. Convection did not fully develop and the situation evolved rapidly toward a stably stratified state. This was due to the fact that upward motions do not release latent heat in unsaturated air (as derived from the environmental conditions), so that strong negative temperature perturbations appeared soon in the updraft and the resulting strong negative buoyancy led to a very fast decrease of the vertical motions. Adding the retrieved temperature perturbations (Fig. 3) to the initial state (simulation WIND + TEMP, not shown) did not change this evolution, as these values were rapidly overwhelmed by the much larger ones resulting from the dry adiabatic vertical motions in unsaturated air.

c. Simulation QVSAT

When the saturated humidity field was used with the Doppler-derived winds (simulation QVSAT), convection developed but the simulated system bore little resemblance with the observed one (Fig. 4). In this case, the circulation reversed with new cells developing toward the line's left (southern) side, while the flow entering from the right (north), being cooled and moistened by precipitation, progressively loses its convective instability. Hence, we are facing the same kind of problem as for simulation WIND, that is, a discrepancy between the wind and the moisture fields. No evaporation was possible in the saturated RTF flow. In these conditions, the low-level flow could not be cooled and it became as unstable as the flow entering from the right (north) of the domain. Likewise, adding the retrieved temperature perurbations (simulation QVSAT + TEMP, not shown) or the specified cloud water contents (simulation QVSAT + CLOUD, not shown) to the initial state did not substantially change the above results, as these imposed perturbations, being not related to the numerically simulated physical processes, have little or no influence on the evolution. It can therefore be concluded that a realistic description of the initial humidity field is necessary to obtain a simulated system coherent with radar observations.

d. Simulation CONTROL

After being initialized with the Doppler-derived winds and the more appropriate distribution of water vapor described in section 4a, the model was integrated over a period of 6 h. The simulated wind and precipitation fields at six successive times are shown in Fig. 5. As compared to the previous experiments, the main characteristic is the stationarity of the low-level RTF flow. This unsaturated flow was first slightly lifted, but,

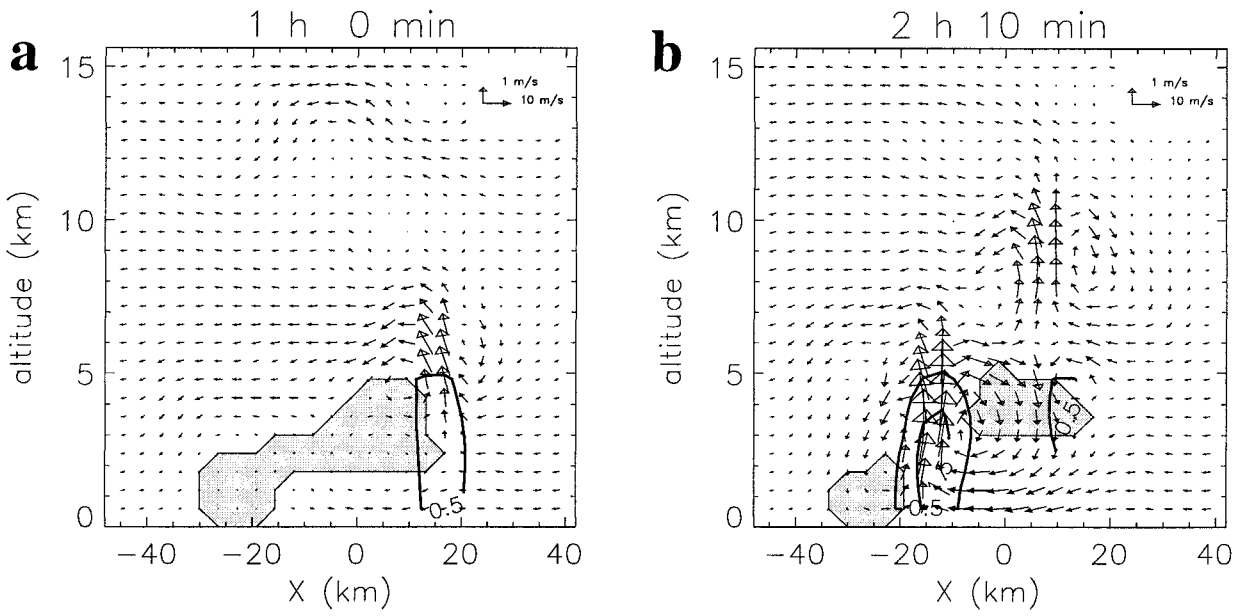

FIG. 4. Wind and total precipitation (rain + snow + graupel) fields for the QVSAT run at (a) 1 h and (b) 2 h 10 min of simulation time. Shaded zones indicate low-level (below 6-km altitude) RTF flow. Contour step for the precipitation content is 1 g kg^{-1}, starting from 0.5 g kg^{-1}.

being cooled by evaporation of precipitation from the updraft, it was then pulled down toward the surface by strong negative buoyancy after a little more than 1 h of simulated time. Figure 5 also shows that the vertical velocity field evolved during the considered period. At the beginning of the simulation, the initial radar-derived up- and downward motions progressively decreased. Then, after about 1 h, a well-organized updraft–downdraft structure established, similar to that derived from the radar data at the earlier times (Figs. 2a and 2b). Vertical velocity in the updrafts showed two maxima near 5- and 10–12-km altitudes. Convective motion rose up to 15-km altitude, with the upper part of the mean ascent sloping toward the left (southern) part of the domain after 2 h. Then, the system progressively weakened and decayed, as did the observed one (Figs. 2d and 2e). Concerning the associated precipitation field, before about 2 h, rain, snow, and graupel formed a rather symmetric structure centered on the convective core. As the storm matured, a more asymmetrical structure developed and the precipitating region in the upper levels progressively leaned toward the left (southern) part of the domain. Near the end of the simulated period, the maximum precipitation content at 7-km altitude is found about 45 km south of the maximum rain content at low levels. Simulation CONTROL-2.4 was identical to the CONTROL one, except a grid spacing of 2.4 km was used (Fig. 6). Except for slightly smaller (and probably more realistic) vertical velocities and precipitation contents aloft before 3 h, both simulations show very similar features, indicating that horizontal grid spacing was probably not a critical parameter here.

As seen in the evolution of the maximum and minimum vertical velocity values (Fig. 7a), the updraft increased during the first 1 h 30 min, up to a maximum of 8 m s^{-1}, it decreased thereafter, however, with two secondary maxima of 5.3 m s^{-1} at 2 h 15 min and 2.5 m s^{-1} at 4 h. The strongest downdraft (-3.5 m s^{-1}) also occured at 1 h 30 min, but its intensity rapidly decreased to -1.2 m s^{-1} at 2 h 15 min. Concerning the mean water mixing ratios (Fig. 7b), the rain (q_r) and graupel (q_g) values grew rapidly during the first hour. The largest mean rain content (1 g kg^{-1}) was observed at 1 h, while the graupel content continued to grow up to 2 g kg^{-1} at 1 h 30 min, at the same time as the upward velocity was maximum. The mean snow mixing ratio (q_s) reached a smaller maximum of 0.7 g kg^{-1} at 1 h 40 min, at the same time as cloud ice q_i. Then, all the mean water contents, including cloud water q_c, decreased to 0.25–0.5 g kg^{-1} at 5 h. The first secondary maximum of upward velocity at 2 h 15 min was associated with small inflexions of the decreasing cloud ice, graupel, and snow mixing ratios.

More details on the evolution of the microphysical fields are given in Fig. 8. Cloud water (Figs. 8a–c) was mainly produced in the updraft below 6-km altitude ahead of and above the low-level RTF flow. On the contrary, cloud ice (Figs. 8d–f) was found between 6 and 15 km in the upper part of the updraft, the southward propagation of which caused a similar dispacement of the cloud ice zone. An extensive anvil was rapidly produced above 13-km altitude and it remained there throughout the considered period. The graupel field (Figs. 8g–i) was well correlated with the upper-level

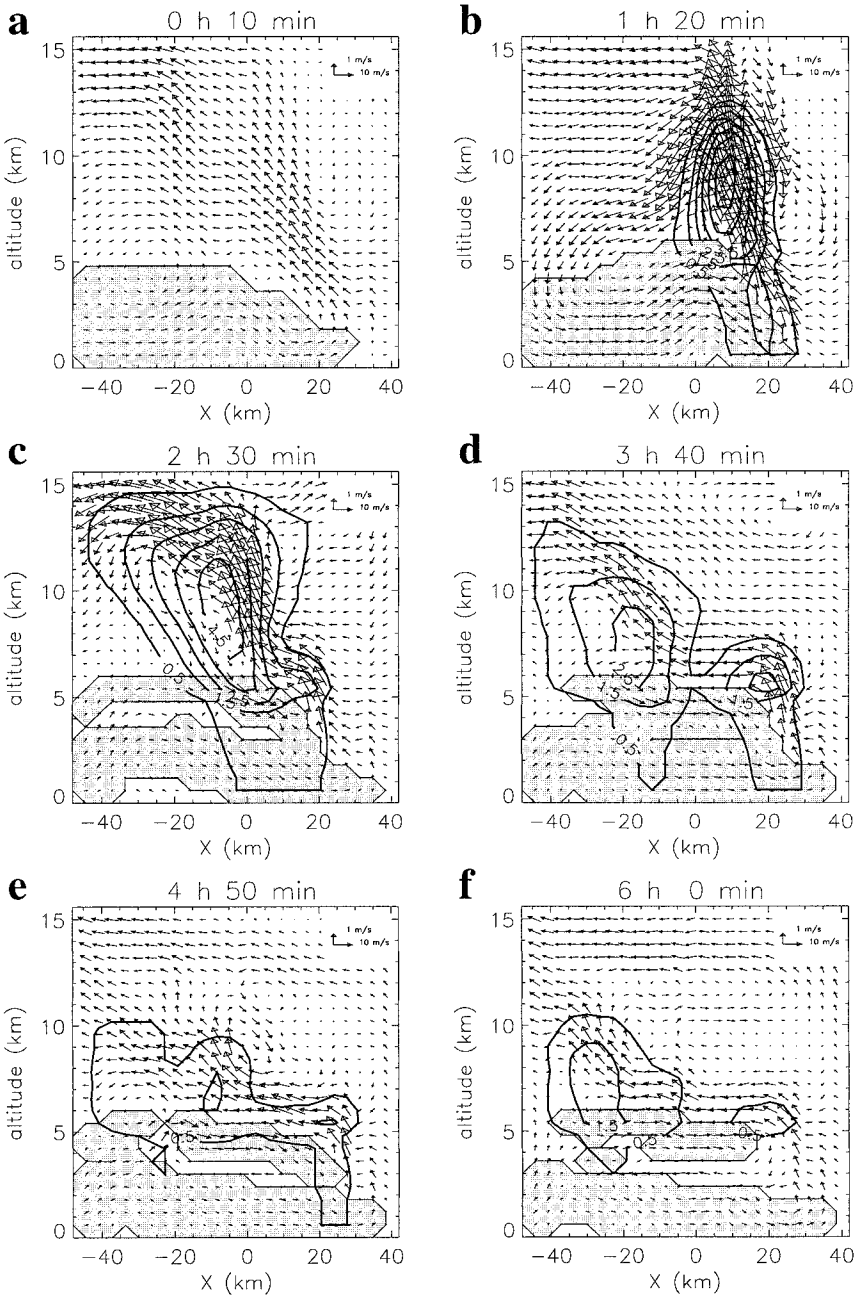

FIG. 5. As in Fig. 4 except for the CONTROL run at (a) 0 h 10 min, (b) 1 h 20 min, (c) 2 h 30 min, (d) 3 h 40 min, (e) 4 h 50 min, and (f) 6 h of simulation time.

updraft and the cloud ice content. It intensified rapidly with peak values >4 g kg^{-1} at 9-km altitude at 2 h 30, then weakened and shrank progressively while moving southward. The snow fields (Figs. 8j–l) showed relatively similar features and evolution as the graupel ones, except for smaller intensity and lower altitudes of the maxima (e.g., 1.6 g kg^{-1} at 11-km altitude at 2 h 30 min). Rainwater (Figs. 8m–o) showed a first maximum in the leading part of the RTF flow, probably in relation with the cloud water maximum. With time, the melting of graupel and snow aloft becomes the main source of rainwater and the maximum shifted southward.

The associated temperature and moisture perturbations with respect to the environmental values at two simulation times (2 h 30 min and 6 h) are displayed in Fig. 9. At 2 h 30 min, temperature perturbations reveal low-level cooling (≥ -2 K) and warming (≤ 3 K) above 5-km altitude (Fig. 9a). Humidity perturbations show a localized minimum ≥ -1 g kg^{-1}) at $5 < X < 20$ km below 2-km altitude, and positive perturbations (<2.5

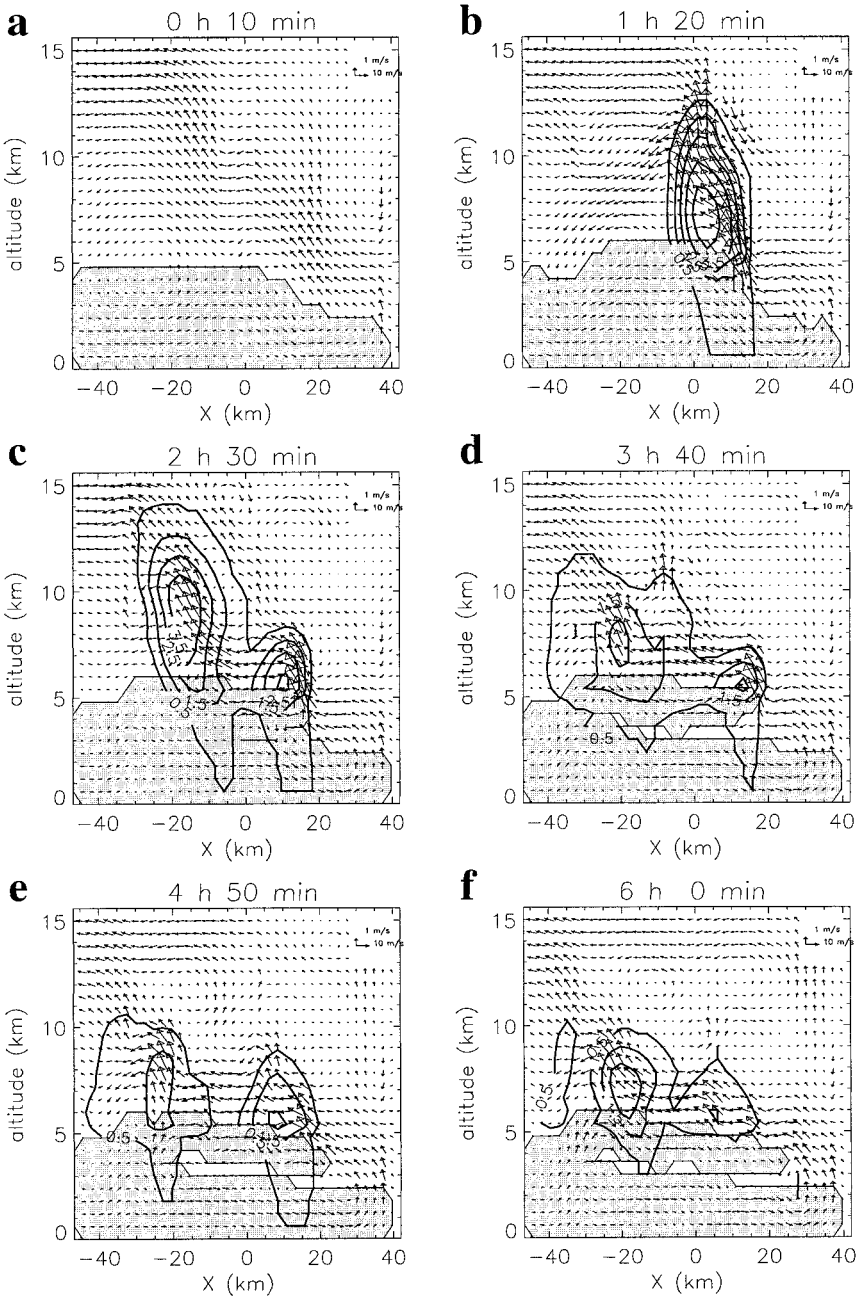

FIG. 6. As in Fig. 5 except for a horizontal grid spacing of 2.4 km.

g kg^{-1}) everywhere else, except in the inflow region ($X > 30$ km) aloft (Fig. 9c). Comparisons with Fig. 5c indicate that warming and moistening were due to the upward transport of water vapor and its subsequent condensation into cloud water and cloud ice within the main updraft, while cooling resulted from the melting of iced hydrometeors below the level of the 0°C isotherm at 4.8 km and from the evaporation of rain in the unsaturated RTF flow in the lowest levels (note that a moisture perturbation up to $+2$ g kg^{-1} was not enough to saturate this flow, as it can be seen on the sounding displayed in Fig. 1a). At 6 h, although the low-level cooling did not change much with ≥ -2 K temperature perturbations, the values obtained above 5-km altitude were much smaller (≤ 1 K) with negative perturbations (< -1 K) above 10-km altitude (Fig. 9b). The moisture perturbation field (Fig. 9d) was more stationary, with, however, slightly stronger low-level drying (≥ -2 g kg^{-1}) and smaller moistening above.

The structure and evolution displayed for CONTROL simulation is fairly coherent with that displayed by the radar-derived wind, reflectivity, and retrieved temper-

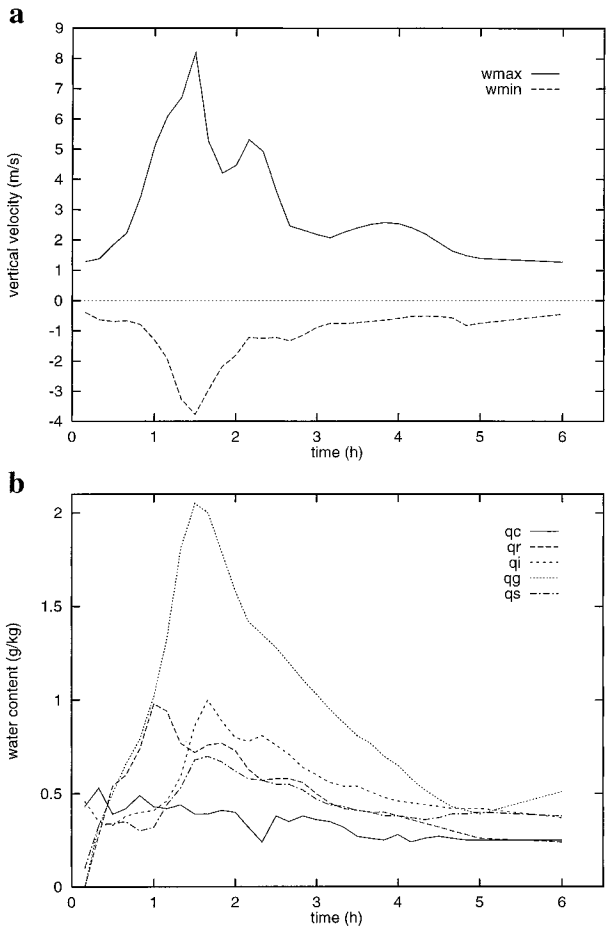

FIG. 7. Evolution of (a) the maximum and minimum vertical velocities, (b) the average of the different water contents over the area where hydrometeors are present, for CONTROL run.

ature fields (Figs. 2 and 3). In both cases, strong convective motions developed ahead of the low-level RTF flow, leading to the formation of intense precipitation. Then, as vertical velocities progressively decreased, the upper part of the updraft and the associated precipitation shifted southward while weaker upward motions resulted from forced ascent ahead of the RTF flow, which was cooled by melting and evaporation of precipitation.

There are, however, differences in intensity and evolution of the simulated and observed fields. First, intensity of the simulated vertical motions and precipitation contents is significantly higher than the observed ones. This is certainly due to the fact that the radar-derived two-dimensional fields have been obtained through spatial and temporal averages, extrapolations and filtering, and then adjustments to streamfunctions. These successive steps led to a substantial reduction of the wind intensity. As a matter of fact, whereas the flight-level data showed maximum vertical motions up to 15 m s^{-1} (Smull et al. 1996) and radar-derived three-dimensional fields had strongest updrafts up to 7 m s^{-1} (Roux 1998), the highest vertical wind in the two-dimensional fields was only 4 m s^{-1}. Hence, it is not surprising that the simulated two-dimensional circulation was stronger than the radar-derived one. The same is probably true concerning the apparently slower evolution of the simulated fields. However, the time series shown in Figs. 2 and 3 has been derived from radar data collected between 1635 and 1905, a period during which the MCS underwent an evolution not unlike that displayed by the simulated fields between 2 h 30 min and 4 h 50 min (Figs. 5c–e).

e. Simulation NOICE

The results of the NOICE experiment (Fig. 10) reveal the importance of ice-phase microphysics in the storm structure and evolution. Although the first 2 h of simulation are relatively similar to the CONTROL run, significant differences in the dynamics and the water contents are found at later times. In the NOICE simulation, the main updraft was shallower and slightly less intense, in relation with the lack of additional latent heat released aloft during solid condensation and freezing of liquid into iced hydrometeors. However, the NOICE precipitation contents were not very different from the CONTROL ones below 4 km altitude, while they were much smaller above. It can also be seen in Fig. 10 that the southward shift of the precipitation zone in the NOICE experiment was due to the similar propagation of the main updraft, whereas in the CONTROL run, this resulted from melting of iced hydrometeors falling from above (e.g., compare Figs. 5d and 10d). The low-level RTF and mid- to upper-level FTR flows in the NOICE simulation were slightly weaker than those obtained for the CONTROL run. This was certainly related to the weaker latent heat released aloft and evaporation of precipitation in the low-level RTF flow.

More details on the cloud and rain contents for the NOICE run are shown in Fig. 11. As compared with the similar Fig. 8 for the CONTROL simulation, there are many more differences in precipitation than in cloud content (including liquid and ice cloud for the CONTROL). The slower ice-phase microphysical processes in the CONTROL run allowed the formation and southward advection of precipitation aloft from the cloud content generated in the updraft, whereas in the NOICE simulation, the nearly equivalent cloud water amount was transformed into rain that precipitated rapidly due to the larger fall speed.

Similar conclusions on the impact of ice-phase microphysics in simulated squall line systems were obtained by Szeto and Cho (1994) and Liu et al. (1997). They found that the low-level RTF flow was weaker and shallower, the convective up- and downdrafts were less intense, the distribution of precipitation away from the convective updraft was less important, and the simulated system decayed more rapidly when only the warm rain processes were taken into account.

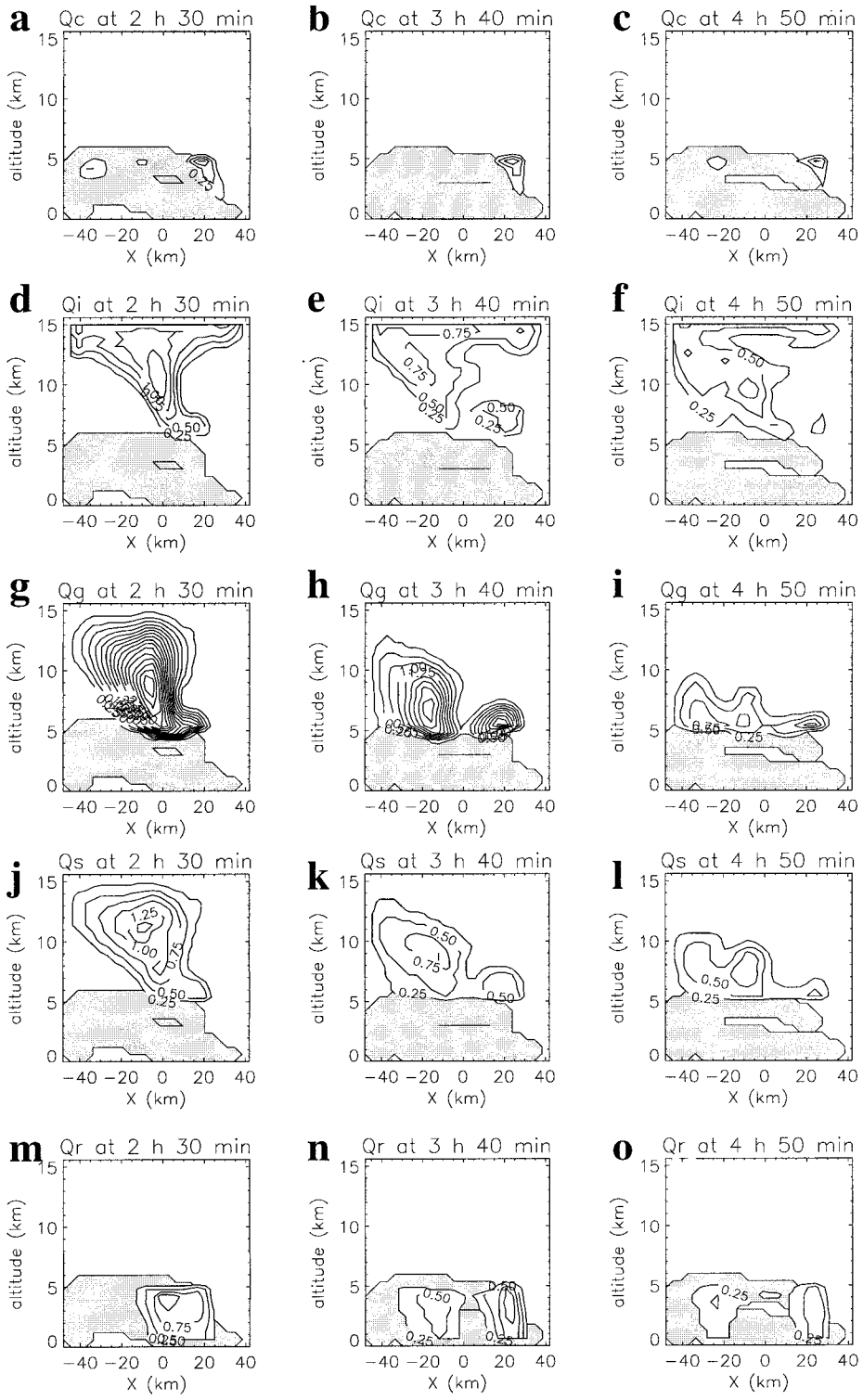

FIG. 8. Microphysical fields for the CONTROL run: cloud water mixing ratio q_c at (a) 2 h 30 min, (b) 3 h 40 min, (c) 4 h 50 min; cloud ice mixing ratio q_i at (d) 2 h 30 min, (e) 3 h 40 min, (f) 4 h 50 min; graupel mixing ratio q_g at (g) 2 h 30 min, (h) 3 h 40 min, (i) 4 h 50 min; snow mixing ratio q_r at (j) 2 h 30 min, (k) 3 h 40 min, (l) 4 h 50 min; rain mixing ratio q_r at (j) 2 h 30 min, (k) 3 h 40 min, (l) 4 h 50 min. Shaded zones indicate low-level (below 6-km altitude) RTF flow. Contour step is 0.25 g kg^{-1}.

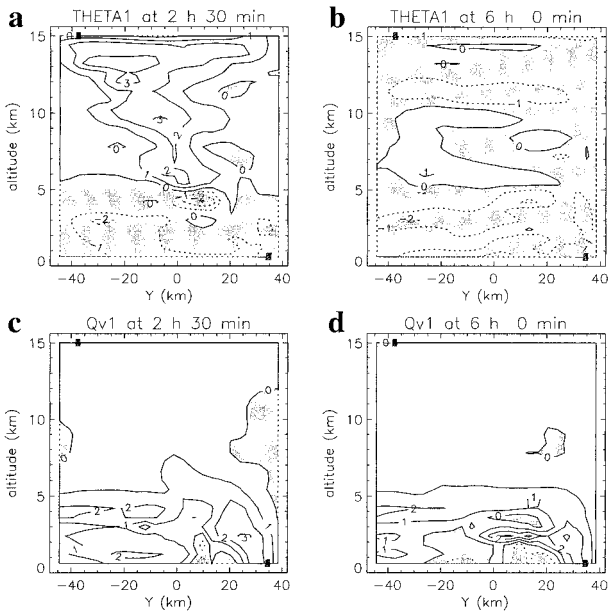

FIG. 9. Potential temperature perturbations (in K) at (a) 2 h 30 min, (b) 6 h, and water vapor perturbations (in g kg^{-1}) at (c) 2 h 30 min, (d) 6 h, for the CONTROL run.

f. Simulations TEMP and CLOUD

The qualitative and quantitative characteristics of the simulated system for the TEMP experiment (not shown) were nearly identical to those for the CONTROL run. The only noticeable difference was that the RTF flow stabilized slightly earlier, probably because of the small negative buoyancy associated with the negative temperature perturbations retrieved in the lowest levels. However, once precipitation began to evaporate in the unsaturated RTF flow, the induced cooling overwhelmed the smaller retrieved temperature perturbations.

Likewise, the CLOUD run (not shown), where an initial cloud content was used, displayed no significant change with respect to the CONTROL experiment. This can be explained by the very high humidity in the tropical oceanic environment. Condensation of water vapor into cloud water and cloud ice is a very fast process, as soon as upward motions occur in saturated conditions. Therefore, adding relatively small initial cloud water contents (less than 1 g kg^{-1}) to this large humidity reservoir did not change much of the simulated microphysical, and dynamic, processes.

g. Simulations RAD and SFLUX

The experiment RAD was started from the CONTROL run at 2 h, when the radiation scheme was activated. The simulation was then continued for 2 h. The observed evolution (not shown) of the maximum and minimum values of vertical velocity, as well as the mean water contents, was nearly identical to that obtained for the CONTROL run. There were no significant differences in the temperature and humidity perturbation fields. This is possibly a result of the fact that 2 h was not enough simulation time for the small, but persistent, radiative cooling in the upper troposphere to significantly change the behavior of the system.

Likewise, turning the surface flux parameterization scheme on at the beginning of the simulation, with the same initial conditions as the CONTROL run, did not lead to significant differences after 6 h of integration. A rather similar result was found for the case of the 22 February 1993 squall line during TOGA COARE by Wang et al. (1996) and Trier et al. (1996), who concluded that the influence of the MCS-induced surface fluxes and stresses is limited to the later stages (>5 h) of simulation.

6. Discussion and conclusions

We have presented results from the numerical simulation of an oceanic tropical mesoscale convective system obtained with a nonhydrostatic cloud-resolving model initialized with kinematic, thermodynamic, and microphysical fields derived from airborne Doppler radar observations and radiosounding data. As this was mainly a feasibility study and in order to more easily test different approaches, two-dimensional fields representing the mean atmospheric circulation in a vertical plane normal to the MCS major axis were used for this purpose.

Firstly, we faced the same problem as Lin et al. (1993) did in their study of the initialization of the 20 May 1977 Del City tornadic storm with multiple ground-based Doppler radars. As radar-derived wind and reflectivity fields can be obtained only in irregular domains and numerical cloud models cannot handle data void regions, it is necessary to fill these areas. This was achieved using a wind profile derived from radiosounding and flight-level data, and an adjustment procedure to ensure smooth transitions between the different domains. As discussed by Lin et al. (1993), this may cause some errors in regions where radar reflectivity is below some threshold but the wind field differs substantially from the environmental values (i.e., rain-free up- or downdrafts, regions where microwave attenuation is strong, etc.). In the present case, intensity of the upward and downward motions was not strong enough to cause the hydrometeors to be totally lifted or to completely evaporate. Moreover, the maximum of the values measured within each grid box by the radars aboard three aircraft flying different trajectories was used to calculate the three-dimensional reflectivity fields, which should therefore not have been too severely distorted by attenuation. But, due to the fact that airborne Doppler radar operate at attenuating wavelengths (about 3 cm), it is highly possible that an unknown *global* bias existed in the reflectivity fields and the derived precipitating water contents.

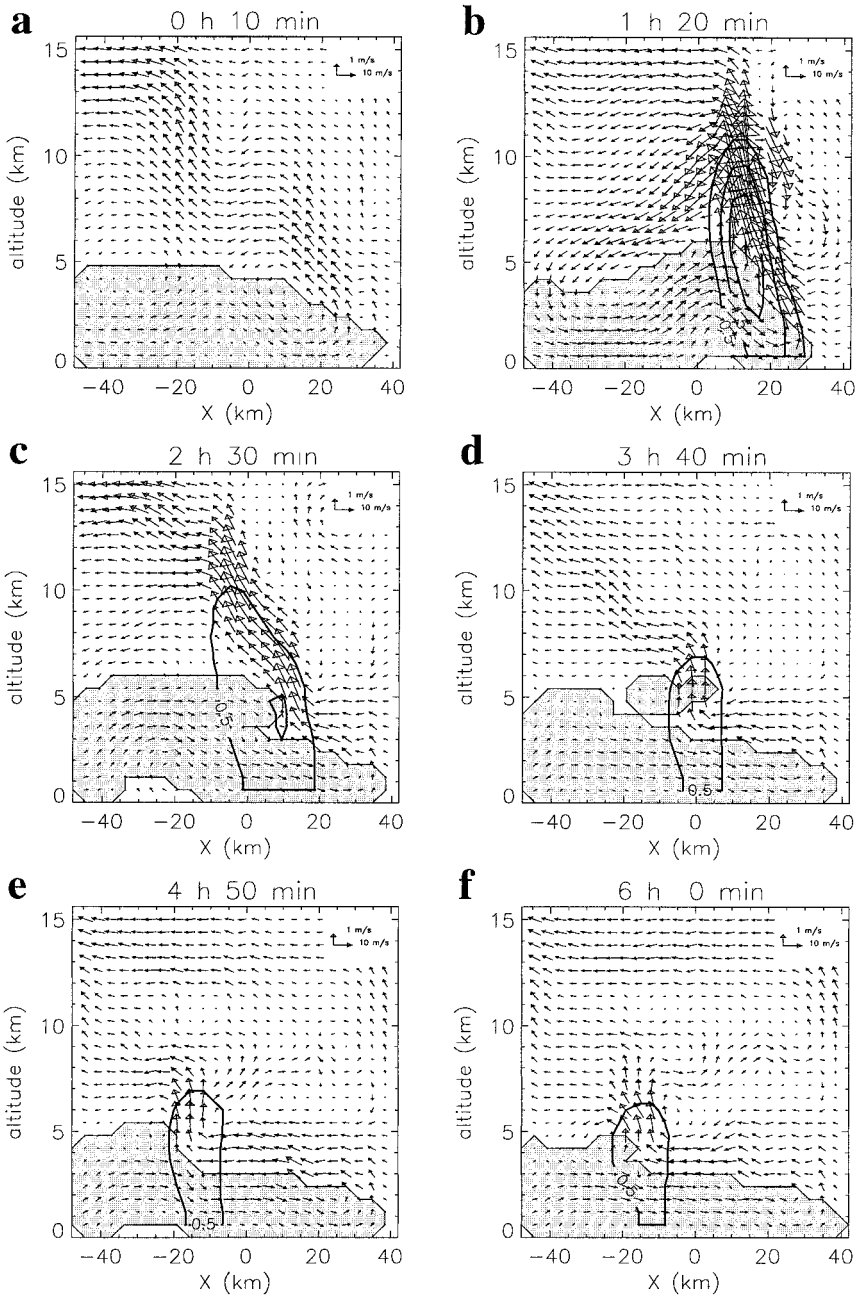

FIG. 10. As in Fig. 4 except for the NOICE run at (a) 0 h 10 min, (b) 1 h 20, (c) 2 h 30 min, (d) 3 h 40, (e) 4 h 50 min, and (f) 6 h of simulation time.

These required preliminary analyses imply that the numerical model was not initialized with an instantaneous ''snapshot'' of the kinematic, thermodynamic, and microphysical variables, but with averaged and smoothed two-dimensional fields. Therefore, we did not attempt to reproduce the observed details of structure and evolution of the different variables, but to verify the overall consistency of the simulated fields. As a matter of fact, the main objective of this study was to determine which parameters are crucial and which ones are relatively less important, so as to obtain as realistic simulations as possible. Unfortunately, Doppler radars directly provide only a limited set of parameters (reflectivity values from which precipitation contents are estimated, radial velocities from which Cartesian wind components are calculated), while the other ones, which are necessary to have a coherent set of variables, can only be ''retrieved'' (temperature perturbations) or estimated (water vapor and nonprecipitating water contents). An additional problem concerns the time required

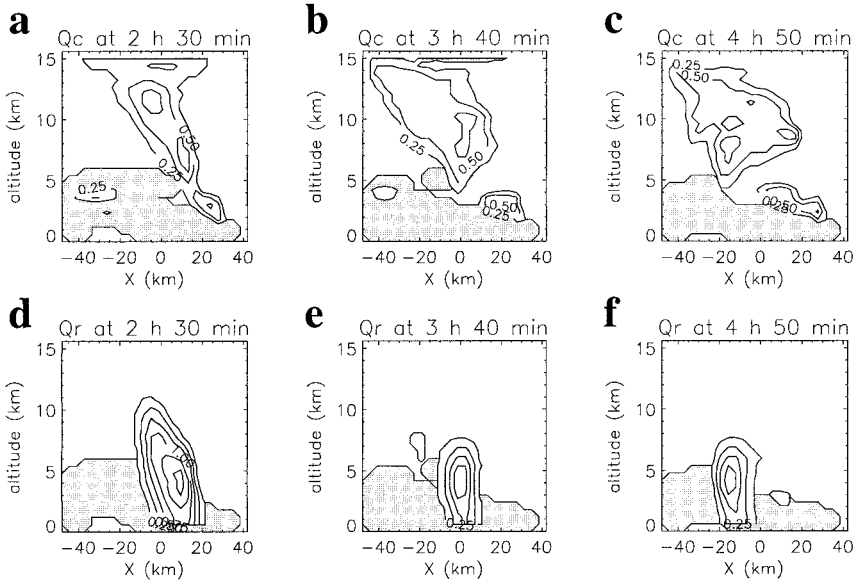

FIG. 11. Microphysical fields for the NOICE run: cloud water mixing ratio q_c at (a) 2 h 30 min, (b) 3 h 40 min, (c) 4 h 50 min; rain mixing ratio q_r at (d) 2 h 30 min, (e) 3 h 40 min, (f) 4 h 50 min. Shaded zones indicate low-level (below 6-km altitude) RTF flow. Contour step is 0.25 g kg^{-1}.

for a ground-based or airborne Doppler radar to scan the considered volume. Data collected during a typical period of 10 min or more have to be ''mixed'' to deduce three-dimensional wind and reflectivity fields. Hence, radar-derived data differ inherently from model-derived fields, as the latter ones actually represent instantaneous states of the simulated atmosphere, while the former ones refer to ''averages'' over the considered period with superimposed observational noise.

Despite the above problems and uncertainties, the first important result we obtained was that the MESO-NH numerical model can be initialized with a two-dimensional wind field describing a well-developed convective circulation. For all the simulations discussed here, it took less than 1 h of simulation time for the model to adapt to this initial input and to generate its own dynamics, leading or not to a deep convective circulation. No spurious wind oscillations were generated, as long as a relatively large horizontal grid spacing ($\geq$2 km) fitting the estimated spectral characteristics of the radar-derived wind field was used. Although similar conclusions were reached by Lin et al. (1993) for a tornadic storm, Crook (1994) and Crook and Tuttle (1994) for simulated and actual gust front data, and Sun and Crook (1996, 1997) for simulated and observed convective storms, there are enough differences between the previous case studies and the oceanic tropical MCS considered here to bring additional support to this approach.

A major conclusion from this study is that, apart from the horizontal and vertical wind, the most important parameter in the initial field is humidity. Realistic simulations could only be obtained when air in the updraft was saturated, so that condensation of water wapor into cloud or cloud ice could release enough latent heat to support the imposed upward motions, and if unsaturated zones were correctly specified, so that cloud and precipitation could evaporate and cool the associated RTF flow. However, even a relatively crude thermodynamic and microphysical description was sufficient: adding temperature perturbations or cloud contents did not bring significant improvements. But inadequate conditions (i.e., unsaturated updraft or saturated low-level RTF flow) led inevitably to unrealistic simulations. This is coherent with the findings by Lin et al. (1993) that an accurate estimate of the low-level water vapor field is needed, and by Sun and Crook (1997, 1998) that errors in estimation of rain mixing ratio from the reflectivity observations and in parameterization of the microphysical processes can result in significant errors. We found that a *complete* description of the saturated/unsaturated conditions is essential, although it does not need to be very accurate (we specified 80% and 100% relative humidity values for the unsaturated and saturated regions, respectively). Here, such a description was based on the calculated ''production rate of precipitation.'' More specifically, ''microphysical retrieval'' techniques (e.g., Rutledge and Hobbs 1983; Hauser et al. 1988; Geerts and Hobbs 1991) could provide improved estimates of humidity, hydrometeors, and temperature in equilibrium with the ambient moisture profile and the radar-derived wind and reflectivity fields.

The fact that a deep convective circulation could be simulated only when the model was initialized with the radar-derived winds and the associated humidity field deserves some comments. As discussed in Roux (1998),

the Geostationary Meteorological Satellite infrared images revealed that the MCS observed with the airborne Doppler radars on 9 February 1993 was not an isolated entity. It was in fact a part of a larger-scale cloud cluster envelope that could be seen in the satellite images from 0945 till 2345 and was formed of successive mesoscale elements that grew and decayed during this period. It is therefore plausible to suppose that the onset of the observed MCS could have resulted from the release of convective instability by forced lifting ahead of a pre-existing cold pool, the characteristics of which would have been approximately simulated by the radar-derived fields. It is to be noted that, from 1615 till 1700, flight-level measurements (not shown) by NOAA P3 N43RF aircraft south of the MCS at about 320-m altitude revealed the presence of zones 30–40-km long with equivalent potential temperature 5–10 K colder than the environmental value (about 345 K), which could be clues of a pre-existing cold pool.

In their simulation of the 22 February 1996 squall line observed during TOGA COARE, Trier et al. (1996) reached a similar conclusion regarding the initialization of their model with a strong prescribed cold pool. The fact that they succeeded in initializing their model with a cold temperature anomaly, whereas such a procedure was found ineffective here, could be related to the different wind profiles, as the CAPE values (about 1500 J kg^{-1}) were almost identical. On 22 February 1993, a low-level jet of 12 m s^{-1} centered at 2-km altitude was certainly an essential feature for the development of the observed (and simulated) squall line, the major axis of which was nearly perpendicular to the vertical wind shear beneath the jet. On 9 February (Fig. 1), the maximum wind was only 7.5 m s^{-1} at 1.5-km altitude and the low-level shear was 3.4×10^{-3} s^{-1} about twice as small as on 22 February, and it was significantly less perpendicular to the MCS main axis. In these conditions, deep convective motions could less easily develop and organize in the absence of a strong forcing such as the radar-derived circulation.

Finally, the relatively limited size of the domain (80-km long) within which the numerical simulations were conducted may raise some concern about the reliability of the obtained results. We must first recall that this domain has been chosen so as to fit the region where radar-derived wind and reflectivity values were available, and to limit the data void areas where a necessarily subjective filling procedure had to be used. In this context, the fact that radar observations are restricted to the regions where there are enough hydrometeors to return detectable signal is a relatively severe limitation. To overcome this difficulty, the radar data could be objectively combined with associated ''clear-air'' measurements, such as radiosounding, dropsonde, or wind profiler data, so as to determine multiscale fields that could then be used to initialize a numerical model. Such a method is under develoment and will be tested using the data collected during the recent Fronts and Atlantic Storm-Track Experiment (Joly et al. 1997), during which airborne Doppler measurements and extensive dropsonde samplings were coordinated to observe the mesoscale structure of Atlantic midlatitude cyclones.

Acknowledgments. The authors are grateful to Dr. Peter Bechtold, Ms. Jacqueline Duron, Dr. Jean-Pierre Pinty, and Dr. Evelyne Richard for their valuable assistance and advice with the MESO-NH model. The comments and suggestions made by two anonymous reviewers helped to improve the paper. The airborne Doppler data were provided by NOAA and NCAR. Calculations were conducted on the computers of Institut du Développement et des Ressources en Informatique Scientifique (IDRIS) through projects IDRIS 950591, 960591, and 970591. This study was supported by Grants INSU/PATOM 96/02 and 97/05.

REFERENCES

Barnes, G. M., and K. Sieckman, 1984: The environment of fast and slow moving tropical mesoscale convective cloud lines. *Mon. Wea. Rev.,* **112,** 1782–1794.

Charnock, H., 1955: Wind stress on a water surface. *Quart. J. Roy. Meteor. Soc.,* **81,** 639.

Cressman, C. W., 1959: An operational objective analysis system. *Mon. Wea. Rev.,* **87,** 367–374.

Crook, A., 1994: Numerical simulations initialized with radar-derived winds. Part I: Simulated data experiments. *Mon. Wea. Rev.,* **122,** 1189–1203.

——, and J. D. Tuttle, 1994: Numerical simulations initialized with radar-derived winds. Part II: Forecasts of three gust-front cases. *Mon. Wea. Rev.,* **122,** 1204–1217.

Deardorff, J. W., 1975: The development of boundary layer turbulence models for use in studying the severe storm environment. *Proc. SESAME Open Meeting,* Boulder, CO, NOAA Environmental Research Laboratories, 251–264.

Emanuel, K. A., 1994: *Atmospheric Convection.* Oxford University Press, 580 pp.

Gamache, J. F., R. A. Houze Jr., and F. D. Marks Jr., 1993: Dual-aircraft investigation of the inner core of Hurricane Norbert. Part III: Water budget. *J. Atmos. Sci.,* **50,** 3221–3242.

Geerts, B., and P. V. Hobbs, 1991: Organization and structure of clouds and precipitation in mid-Atlantic coast of the United States. Part IV: Retrieval of the thermodynamic and cloud microphysical structures of a frontal rainband from Doppler radar data. *J. Atmos. Sci.,* **48,** 1287–1305.

Hauser, D., F. Roux, and P. Amayenc, 1988: Comparison of two methods for the retrieval of thermodynamic and microphysical variables from Doppler radar measurements: Application to the case of a tropical squall line. *J. Atmos. Sci.,* **45,** 1285–1303.

Hildebrand, P. H., and Coauthors, 1996: The ELDORA–ASTRAIA airborne Doppler weather radar: High-resolution observations from TOGA COARE. *Bull. Amer. Meteor. Soc.,* **77,** 213–232.

Houze, R. A., Jr., 1993: *Cloud Physics.* Academic Press, 573 pp.

Joly, A., and Coauthors, 1997: Definition of the Fronts and Atlantic Storm-Track Experiment (FASTEX). *Bull. Amer. Meteor. Soc.,* **78,** 1917–1940.

Jorgensen, D. P., B. F. Smull, S. Lewis, and M. A. LeMone, 1996: Structure and momentum fluxes of four TOGA-COARE convective systems observed by airborne Doppler radar. Preprints, *Seventh Conf. on Mesoscale Processes,* Reading, United Kingdom, Amer. Meteor. Soc., 295–297.

Kessler, E., 1969: *On the Distribution and Continuity of Water Substance in Atmospheric Circulation. Meteor. Monogr.,* No. 32, Amer. Meteor. Soc., 84 pp.

Lafore, J. P., and Coauthors, 1998: The MESO-NH atmospheric simulation system. Part I: Adiabatic formulation and control simulations. *Ann. Geophys.*, **16,** 90–109.

Lee, W.-C., and P. H. Hildebrand, 1995: Kinematic and thermodynamic structure of a TOGA-COARE squall line retrieved from the ELDORA data. Preprints, *27th Conf. on Radar Meteorology,* Vail, CO, Amer. Meteor. Soc., 811–813.

——, and ——, 1996: Momentum transport of a TOGA COARE squall line. Preprints, *Seventh Conf. on Mesoscale Processes,* Reading, United Kingdom, Amer. Meteor. Soc., 152–154.

LeMone, M. A., D. P. Jorgensen, and B. F. Smull, 1994: The impact of two convective systems on sea-surface stresses in COARE. Preprints, *Sixth Conf. on Mesoscale Processes,* Portland, OR, Amer. Meteor. Soc., 40–44.

Lilly, D. K., 1990: Numerical prediction of thunderstorms: Has its time come? *Quart. J. Roy. Meteor. Soc.*, **116,** 779–798.

Lin, Y., P. S. Ray, and K. W. Johnson, 1993: Initialization of a modeled convective storm using Doppler radar-derived fields. *Mon. Wea. Rev.*, **121,** 2757–2775.

Lipps, F. B., and R. S. Hemler, 1982: A scale analysis of deep moist convection and some related numerical calculations. *J. Atmos. Sci.,* **39,** 2192–2210.

Liu, C., M. W. Moncrieff, and E. J. Zipser, 1997: Dynamical influence of microphysics on tropical squall lines: A numerical study. *Mon. Wea. Rev.,* **125,** 2193–2210.

Morcrette, J. J., 1990: Impact of changes in the radiation transfer parameterization plus cloud optical properties in the ECMWF model. *Mon. Wea. Rev.,* **118,** 847–873.

Nicholls, M. E., and M. J. Weissbluth, 1988: A comparison of two-dimensional and quasi-three-dimensional simulations of a tropical squall line. *Mon. Wea. Rev.*, **116,** 2437–2452.

Pinty, J. P., 1997: A microphysical scheme for the atmospheric ice. The MESO-NH Atmospheric Simulation System: Scientic Documentation. [Available from Centre National de Recherches Météorologiques, Météo-France, 42 avenue Coriolis, 31057 Toulouse Cedex, France.]

Redelsperger, J. L., and J. P. Lafore, 1988: A three-dimensional simulation of a tropical squall line: Convective organization and thermodynamic vertical transport. *J. Atmos. Sci.*, **45,** 1334–1356.

Roux, F., 1995: Thermodynamic structure and evolution of mesoscale convective systems observed with airborne Doppler radar during TOGA-COARE. Preprints, *21st Conf. on Hurricanes and Tropical Meteorology,* Miami, FL, Amer. Meteor. Soc., 434–436.

——, 1998: The oceanic mesoscale convective system observed with airborne Doppler radars: Structure, evolution and budgets. *Quart. J. Roy. Meteor. Soc.*, **124,** 585–614.

——, and J. Sun, 1990: Single-Doppler observations of a West African squall line on 27–28 May 1981 during COPT 81: Kinematics, thermodynamics and water budget. *Mon. Wea. Rev.*, **118,** 1826–1854.

——, V. Marecal, and D. Hauser, 1993: The 12/13 January 1988 narrow cold-frontal rainband observed during MFDP/FRONTS 87. Part I: Kinematics and thermodynamics. *J. Atmos. Sci.,* **50,** 951–974.

Rutledge, S. A., and P. V. Hobbs, 1983: The mesoscale and microscale structure and organization of clouds and precipitation in midlatitude cyclones. Part VIII: A model for the seeder-feeder process in warm frontal rainbands. *J. Atmos. Sci.,* **40,** 1185–1206.

Smagorinsky, J., 1963: General circulation experiments with the primitive equations. Part I: The basis experiments. *Mon. Wea. Rev.,* **91,** 99–164.

Smull, B. F., D. P. Jorgensen, T. J. Matejka, and M. A. LeMone, 1994: Evolution of precipitation and momentum structure within a slow-moving convective band observed by airborne Doppler radar during TOGA COARE. Preprints, *Sixth Conf. on Mesoscale Processes,* Portland, OR, Amer. Meteor. Soc., 21–24.

——, ——, ——, and ——, 1995: Airborne Doppler radar and in situ measurements of a slow-moving convective band observed during TOGA COARE. Preprints, *21st Conf. on Hurricane and Tropical Meteorology,* Miami, FL, Amer. Meteor. Soc., 428–430.

——, T. J. Matejka, and M. A. LeMone, 1996: Airflow trajectories within a slow-moving convective system observed during TOGA COARE. Preprints, *Seventh Conf. on Mesoscale Processes,* Reading, United Kingdom, Amer. Meteor. Soc., 289–291.

Sun, J., and N. Crook, 1997: Dynamical and microphysical retrieval from Doppler radar observations using a cloud model and its adjoint. Part I: Model development and simulated data experiments. *J. Atmos. Sci.,* **54,** 1642–1661.

——, and ——, 1998: Dynamical and microphysical retrieval from Doppler radar observations using a cloud model and its adjoint. Part II: Retrieval experiments of an observed Florida convective storm. *J. Atmos. Sci.,* **55,** 835–852.

Szeto, K. K., and H. R. Cho, 1994: A numerical investigation of squall lines. Part III: Sensitivity to precipitation processes and the Coriolis force. *J. Atmos. Sci.,* **51,** 1341–1351.

Trier, S. B., W. C. Skamarock, M. A. LeMone, D. B. Parsons, and D. P. Jorgensen, 1996: Structure and evolution of the 22 February 1993 TOGA COARE squall line: Numerical simulations. *J. Atmos. Sci.,* **53,** 2861–2886.

Wang, Y., W. K. Tao, and J. Simpson, 1996: The impact of ocean surface fluxes on a TOGA COARE convective system. *Mon. Wea. Rev.,* **124,** 2753–2763.

Webster, P. J., and R. Lukas, 1992: TOGA COARE: The coupled ocean–atmosphere response experiment. *Bull. Amer. Meteor. Soc.,* **73,** 1377–1416.

Weisman, M. L., W. C. Skamarock, and J. B. Klemp, 1997: The resolution dependence of explicitly modeled convective systems. *Mon. Wea. Rev.,* **125,** 527–548.

Willoughby, H. E., D. P. Jorgensen, R. A. Black, and S. L. Rosenthal, 1985: Project STORMFURY: A scientific chronicle 1962–1983. *Bull. Amer. Meteor. Soc.*, **66,** 505–514.